Title

Smart-phone based computational microscopy using multi-frame contact imaging on a fiber-optic array

Journal

Lab on a Chip, 13(20)

ISSN

1473-0197

Authors

Navruz, Isa
Coskun, Ahmet F
Wong, Justin
et al.

Publication Date

2013

DOI

10.1039/c3lc50589h

Peer reviewed

Published in final edited form as:
Lab Chip. 2013 October 21; 13(20): 4015–4023. doi:10.1039/c3lc50589h.

Smart-phone based computational microscopy using multi-frame contact imaging on a fiber-optic array

Isa Navruz[§,a,b], **Ahmet F. Coskun**[§,a,c,d,e], **Justin Wong**[a,c], **Saqib Mohammad**[a,c], **Derek Tseng**[a,c], **Richie Nagi**[a,c], **Stephen Phillips**[a,c], and **Aydogan Ozcan**[*,a,c,d]

[a]Electrical Engineering Department, University of California, Los Angeles, CA 90095, USA

[b]Department of Electrical and Electronics Engineering, Ankara University, Ankara, Turkey

[c]Bioengineering Department, University of California, Los Angeles, CA 90095, USA

[d]California NanoSystems Institute (CNSI), University of California, Los Angeles, CA 90095, USA

Abstract

We demonstrate a cellphone based contact microscopy platform, termed *Contact Scope*, which can image highly dense or connected samples in transmission mode. Weighing approximately 76 grams, this portable and compact microscope is installed on the existing camera unit of a cellphone using an opto-mechanical add-on, where planar samples of interest are placed in contact with the top facet of a tapered fiber-optic array. This glass-based tapered fiber array has ~9 fold higher density of fiber optic cables on its top facet compared to the bottom one and is illuminated by an incoherent light source, e.g., a simple light-emitting-diode (LED). The transmitted light pattern through the object is then sampled by this array of fiber optic cables, delivering a transmission image of the sample onto the other side of the taper, with ~3× magnification in each direction. This magnified image of the object, located at the bottom facet of the fiber array, is then projected onto the CMOS image sensor of the cellphone using two lenses. While keeping the sample and the cellphone camera at a fixed position, the fiber-optic array is then manually rotated with discrete angular increments of e.g., 1-2 degrees. At each angular position of the fiber-optic array, contact images are captured using the cellphone camera, creating a sequence of transmission images for the same sample. These multi-frame images are digitally fused together based on a shift-and-add algorithm through a custom-developed Android application running on the smart-phone, providing the final microscopic image of the sample, visualized through the screen of the phone. This final computation step improves the resolution and also gets rid of spatial artefacts that arise due to non-uniform sampling of the transmission intensity at the fiber optic array surface. We validated the performance of this cellphone based *Contact Scope* by imaging resolution test charts and blood smears.

Introduction

With more than 6.5 billion cellphone subscribers world-wide, mobile phones have become ubiquitous tools providing emerging opportunities for field-portable imaging, sensing and diagnostics applications with a potential to transform the delivery of healthcare across the globe. Toward this end, there has been considerable effort to develop cell-phone based bright-field and fluorescent microscopes[1-5], flow-cytometers[6], biosensors[7-9], as well as

[*]Correspondence to: Prof. Aydogan Ozcan (UCLA Electrical Engineering Department, Los Angeles, CA 90095; Tel.: (310) 825-0915; ozcan@ucla.edu; http://www.innovate.ee.ucla.edu; http://org.ee.ucla.edu/).
[§]These authors contributed equally to this project.
[e]Present Address: Division of Chemistry and Chemical Engineering, California Institute of Technology, Pasadena, CA, 91125

digital readers for diagnostic tests[10-12] and lab-on-a-chip systems[13], providing a technology platform that can perform multiple tele-medicine[14-42] related functionalities on cell-phones.

To provide a complementary solution toward the same direction, here we demonstrate a novel cellphone based computational microscope, termed as *Contact Scope*, that can image highly dense and connected samples with a spatial resolution of ~1.6 μm over a field-of-view (FOV) of >1.5 mm^2. This field-portable *Contact Scope* (see Fig.1), weighing approximately 76 grams, can create transmission images of samples that are positioned on the top facet of a glass-based tapered fiber-optic array, which has ~ 9 fold higher density of fiber optic cables on its top surface compared to the bottom one. Using an LED illumination, the transmission pattern of the object is directly sampled by the top surface of the fiber taper, with an irregular pitch size of approximately ~ 2.5 μm, and it is guided toward the bottom facet of the fiber-optic array with an overall magnification factor of e.g., M ~ 3. This magnified transmission pattern of the object is then imaged onto the cellphone CMOS (Complementary Metal–Oxide–Semiconductor) imaging chip through the use of an external lens, that is positioned in front of the embedded lens of the cellphone camera unit (see Fig. 1). Keeping the sample and the cellphone camera at a fixed position, the fiber-optic taper is manually rotated with discrete angular increments of e.g., 1-2 degrees without the use of any bulky mechanical stages. The raw contact images are then captured using the cellphone camera for each angular position of the fiber-optic array, creating a series of transmission images (e.g., 10-40 frames) for the same sample. These multi-frame images are digitally merged using a shift-and-add algorithm[43-48] implemented on a custom-developed Android application (see Fig. 2) running on the smart-phone, creating the final microscopic image of the sample that can be visualized and digitally zoomed in through the screen of the phone. We tested the performance of this cellphone based *Contact Scope* by imaging resolution test targets as well as red and white blood cells. Compared to other transmission based microscopes implemented on cellphones,[2,5] the presented approach leverages computation and digital processing to improve the performance of traditional lens-based imaging systems. In this regard, the design and working principles of this multi-frame imaging and fiber optic taper based contact microscopy platform are rather different than the previous approaches[2,5] including our earlier lens-free imaging work[1]. Furthermore, using custom-designed tapers with even denser array of fiber optic cables, the same microscopy concept can be extended to sub-micron spatial resolution over rather large imaging areas. Fluorescent microscopy can also be implemented on the same design using an appropriate thin-film interference filter or using a set of doped fiber optic cables in the taper to block the excitation light, providing various dual-mode imaging opportunities within the same compact imaging platform on the cellphone.

Methods

Overview of the *Contact Scope* platform

In this cellphone based *Contact Scope*, micro-objects are imaged as they are in contact with the top surface of a fiber-optic taper that is coupled to a cellphone camera through a 2-lens imaging system. By manually rotating the fiber-optic taper with discrete angular increments of e.g., 1-2 degrees (while the sample is kept at a fixed position), transmission contact images are captured using the cellphone camera for each angular position of the fiber-optic array. As illustrated in Figure 3, these raw transmission images are then combined through the use of a custom-developed Android application, creating a high-resolution microscopic image of the sample that can be viewed and zoomed in using the cellphone screen.

Imaging Hardware and its Design—Our *Contact Scope* was built on two different cellphones: an Android phone (Samsung Galaxy S II, 8MP Camera with a built-in lens

which has $f_{built\text{-}in}$ = 4 mm) and a Sony-Ericsson phone (Aino, 8MP Camera with $f_{built\text{-}in}$ = 4.65 mm). The comparison of the performances of these two *Contact Scope*s is provided in Figure 4a. By changing the design of the snap-on attachment, the same contact microscopy concept can also be installed on other smart phones such as an iPhone or other Android devices. The 3D housing of our opto-mechanical attachment to the cellphone was designed using Inventor software (Autodesk), and prototyped using a 3D printer (Elite, Dimension).This snap-on attachment to the cellphone also contained off-the-shelf parts comprising a battery (Digikey, N035-ND, button type without heat sink) that is used to power an LED (Digikey, 475-2549-1-ND, 587 nm peak wavelength with 15 nm bandwidth), a light diffuser (Digikey, 67-1845-ND), a fiber-optic taper (Edmund Optics, 55-138), and a plano-convex lens (Edmund Optics, 45-077, focal length 6 mm). To test different magnification factors, we also evaluated 8 mm and 12 mm focal length lenses (Edmund Optics, 65-576, PCX lens kit) by replacing the add-on lens in our opto-mechanical attachment. Figure 4a provides a performance summary of these different lenses for resolution and FOV of our *Contact Scope* installed on two different cellphones (Samsung and Sony-Ericsson).

The specific functions of these optical components in our imaging design can be summarized as: (*i*) The diffuser inserted between the LED and the sample is used to create uniform illumination over the entire FOV of the sample, e.g., 15 mm^2. (*ii*) The plano convex lens, together with the built-in lens of the cellphone, images/relays the bottom surface of the taper to the active area of the cellphone CMOS imager chip. (*iii*) Fiber-optic taper provides a magnification factor of e.g., $M_1 \sim 3\times$ and its top surface serves as an irregular sampling grid that is used for contact imaging.(*iv*) The magnification factor of the fiber-optic taper (M_1) and the magnification factor of the 2-lens based imaging system (M_2) together determine the total magnification of the imaging system, $M = M_1 \cdot M_2$, where the magnification factor of the 2-lens system is given by $M_2 = f_{built\text{-}in}/f_{add\text{-}on}$, where $f_{add\text{-}on}$ is the focal length of the add-on lens (e.g., 6 mm, 8 mm and 12 mm). For example, for our Samsung Galaxy S II based *Contact Scope* ($f_{built\text{-}in}$ = 4 mm) using an add-on lens with $f_{add\text{-}on}$ = 6 mm, 8 mm and 12 mm, the total magnification factor of our computational microscope can be calculated as 2, 1.5 and 1, respectively.

Android Application—For our *Contact Scope*, we developed an Android application running on the smartphone, which operates as follows (see Fig. 2):

(a) The user clicks on the *Contact Scope* icon and starts to run our smart application on the cellphone.

(b) The new window provides two options: either *New Image* or *Instructions*. Once *Instructions* tab is selected, the standard procedures for contact microscopy are displayed. Otherwise, if *New Image* is selected, the user is asked to rotate the fiber-optic taper with discrete angular increments of e.g., 1-2 degrees. For each angular position of the fiber-optic taper the cellphone camera captures a contact transmission image of the samples and saves it on the memory of the phone, creating a series of contact images (e.g., 10-40). Note that it is not essential to rotate the taper with precise angular increments as the digital processing on the cellphone automatically calculates the relative shifts between the raw images, as will be detailed later on.

(c-d) One of these raw contact images is then displayed on the screen for the user to select a region-of-interest (ROI) to apply image-processing and to digitally zoom in. The user can then adjust the size and the position of the selected ROI interactively through finger movements performed on the cellphone screen. Once a ROI is defined and selected, the user can click on the *Process images* tab (Fig. 2) to proceed with the

digital processing of the raw transmission images that were acquired as a function of the taper rotation.

(e) While performing the shift-and-add algorithm through the cellphone, a small window pops up displaying *Processing images*.

(f) The final contact image corresponding to the selected ROI is then displayed on the cellphone screen. If needed, the user can select the *Process New Images* tab to select another ROI of the same specimen.

Shift-and-add algorithm—The raw transmission images acquired by the cellphone camera are digitally merged into a final higher resolution image based on a shift-and-add algorithm (see Fig. 3), the steps of which can be described as follows: (*i*) Raw images are converted into gray scale images by selecting only the green channels of the cellphone CMOS images. (*ii*) Based on a correlation window (size of e.g., 50×50, 100×100 or 150×150 pixels) that is automatically defined by the algorithm, spatial shifts between the raw contact images are estimated. (*iii*) These estimated shifts are then used to digitally realign each raw image FOV with respect to others. (*iv*) These re-aligned transmission images are then added together to create an averaged contact image. (*v*) Wiener deconvolution is applied to this resulting image, cleaning up the spatial artifacts that appear in our images due to non-uniform sampling of the transmission signal at the fiber-optic taper, which then provides the final high-resolution microscopic image displayed on the smart-phone screen.

The above outlined processing for a selected ROI that has a field-of-view of e.g., 0.2 mm^2, takes less than one minute using our custom-designed Android application running on Samsung Galaxy S II, whereas the same reconstruction takes less than 20 seconds through MATLAB running on a PC (2. 80 GHz CPU Processor).

To shed more light on the influence of different parameters in this reconstruction process, in Fig.3(c), for a ROI of 300×300 pixels, the processed contact images of red blood cells are shown as a function of (1) the correlation window (CR) size, ranging from 50×50 to 200×200 pixels, and (2) the number of transmission images/frames, ranging from 10 to 40. These results presented in Fig.3(c) demonstrate that larger correlation windows and more transmission images/frames used for shift-and-add based reconstructions might help us achieve a higher-resolution at the cost of increased computation time. In this work, we typically used a CR size of 150×150 pixels and 30-40 transmission frames to create higher resolution microscopic images, to be further detailed in the Results and Discussion Section.

Sample Preparation—We performed experiments with blood cells smeared on a glass slide, creating a monolayer of cells. To prepare these smear samples, a small volume (e.g., 1 μL) of whole blood sample is treated with 2.0 mg EDTA/mL and then pipetted onto a 1 mm thick glass slide. A cover slip was used to spread and smear the blood over the glass slide at a smearing angle of approximately 30 degrees. Upon drying the smeared specimen in air for 5 minutes, the blood cells were fixed and stained by HEMA 3 Wright-Giemsa staining kit (Fisher Diagnostics). This sample is then dipped (5 times each) into three different Coplin jars, containing HEMA 3 fixative solution, eosinophilic staining solution (HEMA 3 solution I) and basophilic solution (HEMA 3 solution II), respectively. After rinsing the specimen with deionized water and drying with air, the samples were imaged with our *Contact Scope*.

Sample Mounting Procedures—In our *Contact Scope* platform, the specimen that is prepared on a glass slide (see the previous subsection on sample preparation details) is placed on a sample holder. This holder is then brought in soft contact with the base of the mechanical attachment, where the specimen is seated on the top facet of the fiber optic taper.

This soft contact also ensures that the samples do not shift/move or get damaged during the minor rotational movement of the taper surface as part of the image acquisition process. If needed, in certain cases a refractive index matching liquid/oil can also be used to ease the rotation of the taper while also maintaining a decent contact between the sample and the taper surface.

Results and Discussion

We initially evaluated the performance of this *Contact Scope* platform using two different cellphones, including an Android phone and a Sony-Ericsson phone. In this comparison, we quantified the spatial resolution and the FOV using resolution test targets as a function of various add-on lenses (i.e., with focal lengths of 6 mm, 8 mm and 12 mm), keeping the other optical parts including the fiber-optic taper the same. The results presented in Fig. 4(a) demonstrate that the FOV of the Samsung smart-phone based *Contact Scope*, compared to the Sony-Ericsson based one, is slightly larger while the spatial resolution of the same design is slightly worse. For this FOV analysis, we qualitatively define the acceptable area as the portion of the FOV that suffers from spatial aberrations but individual micro-objects can be still identified separately; and the aberration-free area as the centre of the FOV that does not exhibit any noticeable spatial aberrations. We should note that quantified definitions for these terms could also be implemented based on the measurement of the spatial transfer function of our imaging system. In the light of the results summarized in Fig. 4, we conclude that our *Contact Scope* can achieve >1.5-2.5 μm spatial resolution over a FOV of e.g., >1.5-15 mm^2. The spatial resolution of *Contact Scope* is mostly affected by the sampling pitch at the smaller facet of the taper, and by using a denser array of fiber optic cables one can achieve a better resolution, potentially reaching sub-micron level using the same imaging design. To avoid cross-coupling among neighboring fibers, a higher refractive index glass core or metallic cladding layers can be employed within the preform during the taper drawing process. Apart from the sampling pitch at the fiber optic taper, another resolution limitation in this design is due to the gap between the sample plane and the taper end. Even though contact microscopy implies that this physical gap is negligible, it is practically difficult to maintain exact contact with all the points on the sample surface. Therefore rather than sampling the direct transmission of the object, the taper actually samples the diffracted light pattern passing through the specimen, which creates resolution limitations for contact microscopy in general. To mitigate this issue, thicker glass substrates (e.g., >0.5 mm) that exhibit minimal surface curvature can be utilized to practically reduce the gap between the specimen and taper surface for all points on the object plane.

Using *Contact Scope*, we also performed experiments with blood smear samples that contain dense regions of red blood cells (RBCs) and white blood cells (WBCs). The wide-field image of the RBCs acquired using the *Contact Scope* (with the configuration employing an Android cellphone and a 6 mm add-on lens) is illustrated in Fig. 5(I), where the corresponding final high resolution image and a 10× microscope objective (NA = 0.25) comparison of the same FOV are also provided in Figs.5 (II) and (III), respectively. Digitally zoomed parts of this wide FOV image shown in Figs. 5 (I-A) and (I-B) are also processed through the same shift-and-add algorithm (as detailed in our Methods Section), where a CR of 150×150 pixels and 40 transmission frames are used, creating the high-resolution contact images shown in Figs. 5 (II-A) and (II-B) for two different FOVs, respectively. These *Contact Scope* images agree well with their corresponding 10× microscope objective images as demonstrated in Figs. 5(III-A) and (III-B), respectively.

Next we present WBC imaging results (Fig. 6) acquired through the same *Contact Scope*, where the first column demonstrates the raw contact image (i.e., a single frame) corresponding to four different FOVs containing WBCs. These raw transmission frames are

then digitally processed using the Android cellphone through the shift-and-add algorithm as shown in the second and third columns of Fig. 6, providing higher resolution contact images of the same WBCs, where subcellular nuclear features can be resolved. For comparison purposes, bright field microscope images obtained with a 10× objective lens are also shown in the last column of the same figure, providing a decent match to our high-resolution transmission images acquired with *Contact Scope*.

An important promising feature of computational smartphone based microscopes for global health applications is that they can be used to diagnose diseases by assisting micro-analysis on various pathology specimen including for instance blood or Papanicolaou smears and histopathology samples. In addition to their local use as field-portable microscopes, smartphone enabled imaging systems can also be employed to rapidly communicate microscopic data/images along with other patient related information to secure central servers, creating numerous opportunities for various fields including telemedicine and epidemiology, among others.[49-51]

We should emphasize that *Contact Scope* can also perform colour microscopy through the use of a broadband (e.g., white) LED as an illumination source, revealing the natural colour contrast of the objects. Furthermore, the design of the *Contact Scope* can also be modified to create a dual mode imager that can achieve bright field and fluorescent contact microscopy running on the same cellphone using an additional emission filter inserted into the optical detection path of this design. Such a dual mode imager could also be valuable for sensitive and specific imaging of fluorescently labeled samples.

Finally, we should emphasize that the cellphone based contact microscope described in this work constitutes a spatially incoherent imaging modality. In other words, phase information of the specimen is not preserved at the detector end of our imaging system due to spatially incoherent illumination. In general, however, under spatially and temporally coherent illumination, a fiber-optic array based imaging system would be sensitive to the phase of the specimen, and can be used (after appropriate calibration steps) for phase and amplitude imaging of the objects. The same is also true for multi-mode fiber optic cables, which are becoming more and more popular for endoscopic imaging applications. Such multi-mode fiber optic cables (with large core diameters) can be used for computational imaging of specimen after some calibration steps to understand the modal decomposition of input fields or intensities as light propagates within the fiber core. One general challenge in such multi-mode fiber based imaging systems is that this calibration information would depend on the geometry of the fiber, which might introduce spatial artefacts as the fiber orientation changes or gets distorted due to for example bending or temperature gradients. A possible solution for this issue could be to include “guide star” like features within the object field-of-view to dynamically estimate these perturbations and recalibrate the multi-modal imaging system as needed.

In terms of resolution limits of such multi-mode fiber-optic systems, one must carefully consider various important factors. For example, it would be misleading to state that intensity measurement of multi-modal distribution at the exit facet of a fiber optic cable increases the number of resolvable points of the imaging system by a factor of 4 due to mode mixing. Such a conclusion might stem from an incomplete comparison of coherent vs. incoherent imaging systems. A coherent imaging system is linear in fields, and the coupling of the object fields to a multi-mode fiber is sensitive to the 2D phase distribution at the object plane. Stated differently, a coherent imaging system, including the ones that use multi-mode fiber optic cables, can image phase and amplitude information of ***complex objects***, and the transfer function of such coherent systems have spectral widths of $2\times NA/\lambda$, extending from $-NA/\lambda$ to NA/λ, where NA refers to the effective numerical aperture of the

coherent system, and λ refers to the illumination wavelength[52,53]. On the other hand, an incoherent system, or an imaging system that only cares for the amplitude or intensity of an object, would have a broader transfer function, that would extend from -2NA/λ to 2NA/λ. If we count the number of discreet spatial frequencies under the two-dimensional transfer function of an incoherent system, we could find a 4-fold increase compared to the coherent imaging case. This factor of 4 is unfortunately the source of a possible misconception that intensity detection (through mode mixing) creates improved resolution by having more resolvable points through a multi-mode fiber. In fact, the intensity of an object contains more spatial frequencies due to convolution operation in frequency domain. One can better visualize this phenomenon by comparing the frequency spectrum of a cosine function against its intensity, which oscillates twice faster than the cosine frequency. Therefore, as the incoherent transfer function gets seemly wider (with 4× more points) compared to a coherent transfer function, the object intensity also beats faster compared to the complex object field. Therefore, possible claims of increased resolvable points with intensity detection, unfortunately, would miss that the intensity of an object has faster oscillations than its field and a coherent imaging system that utilizes a multi-mode fiber optic cable (despite its narrower spatial bandwidth) deals with a complex object function, where both phase and amplitude distribution at the object plane affect the coupling process to the modes of the fiber.

To summarize the above discussion:

1. One can form a coherent or an incoherent imaging system based on a multi-mode fiber optic cable or an array of fibers, both of which would rely on a careful calibration process for image reconstruction.
2. The coherent one would be able to image the phase and amplitude of a complex object with a spectral transfer function that extends from -NA/λ to NA/λ (with an area proportional to the square of NA/λ).
3. The incoherent one would be able to only image the intensity of the object with a spectral transfer function that extends from -2NA/λ to 2NA/λ. This widening of the transfer function area is balanced by the fact that the intensity of an image contains wider spectrum of spatial frequencies that are above a detection noise floor.
4. An incoherent system introduces artefacts since the higher spatial frequencies within the transfer function are artificially supressed compared to the lower spatial frequencies; a conclusion that is true for any spatially incoherent imaging system.
5. A coherent system suffers from speckle and multiple reflection noise[53] artefacts which spatially superimpose on the reconstructed complex object field.

Therefore a comparison between the resolution limits of a multi-mode fiber optic cable (or an array of fibers) for complex vs. amplitude only objects needs a detailed analysis; and *restricting the sample to an amplitude-only object for a coherent system could create misleading conclusions, and under-utilization of the information capacity of the imaging system*.

Conclusions

We demonstrated a cellphone based computational contact microscopy platform (termed as *Contact Scope*) that can image highly dense and connected samples such as confluent cells and tissue slides. Such a lightweight and compact microscopy tool, utilizing a multi-frame image acquisition scheme and rapid digital processing running on smart-phones, could especially be useful for telemedicine applications.

Acknowledgments

Ozcan Research Group gratefully acknowledges the support of the Presidential Early Career Award for Scientists and Engineers (PECASE), Army Research Office (ARO) Life Sciences Division, ARO Young Investigator Award, National Science Foundation (NSF) CAREER Award, NSF CBET, Office of Naval Research (ONR) Young Investigator Award and National Institutes of Health (NIH) Director's New Innovator Award DP2OD006427 from the Office of the Director, National Institutes of Health.

References

1. Tseng D, Mudanyali O, Oztoprak C, Isikman SO, Sencan I, Yaglidere O, Ozcan A. Lab Chip. 2010; 10:1787–1792. [PubMed: 20445943]
2. Breslauer DN, Maamari RN, Switz NA, Lam WA, Fletcher DA. PLoS ONE. 2009; 4:e6320. [PubMed: 19623251]
3. Zhu H, Yaglidere O, Su TW, Tseng D, Ozcan A. Lab Chip. 2011; 11:315–322. [PubMed: 21063582]
4. Zhu H, Sencan I, Wong J, Dimitrov S, Tseng D, Nagashima K, Ozcan A. Lab Chip. 2013; 13:1282–1288. [PubMed: 23392286]
5. Smith ZJ, Chu K, Espenson AR, Rahimzadeh M, Gryshuk A, Molinaro M, Dwyre DM, Lane S, Matthews D, Wachsmann-Hogiu S. PLoS ONE. 2011; 6:e17150. [PubMed: 21399693]
6. Zhu H, Mavandadi S, Coskun AF, Yaglidere O, Ozcan A. Anal Chem. 2011; 83:6641–6647. [PubMed: 21774454]
7. Zhu H, Sikora U, Ozcan A. Analyst. 2012; 137:2541–2544. [PubMed: 22396952]
8. Gallegos D, Long KD, Yu H, Clark PP, Lin Y, George S, Nath P, Cunningham BT. Lab Chip. 2013; 13:2124–2132. [PubMed: 23609514]
9. Preechaburana P, Gonzalez MC, Suska A, Filippini D. Angew Chem Int Ed. 2012; 51:11585–11588.
10. Coskun AF, Wong J, Khodadadi D, Nagi R, Tey A, Ozcan A. Lab Chip. 2013; 13:636–640. [PubMed: 23254910]
11. Mudanyali O, Dimitrov S, Sikora U, Padmanabhan S, Navruz I, Ozcan A. Lab Chip. 2012; 12:2678–2686. [PubMed: 22596243]
12. Shen L, Hagen JA, Papautsky I. Lab Chip. 2012; 12:4240–4243. [PubMed: 22996728]
13. Ruano-López JM, Agirregabiria M, Olabarria G, Verdoy D, Bang DD, Bu M, Wolff A, Voigt A, Dziuban JA, Walczak R, Berganzo J. Lab Chip. 2009; 9:1495–1499. [PubMed: 19458852]
14. Kim SB, Bae H, Cha JM, Moon SJ, Dokmeci MR, Cropek DM, Khademhosseini A. Lab Chip. 2011; 11:1801–1807. [PubMed: 21483937]
15. Dimov IK, Basabe-Desmonts L, Garcia-Cordero JL, Ross BM, Ricco AJ, Lee LP. Lab Chip. 2011; 11:845–850. [PubMed: 21152509]
16. Dimov IK, Kijanka G, Park Y, Ducree J, Kang T, Lee LP. Lab Chip. 2011; 11:2701–2710. [PubMed: 21709914]
17. Gansen A, Herrick AM, Dimov IK, Lee LP, Chiu DT. Lab Chip. 2012; 12:2247–2254. [PubMed: 22399016]
18. Myers FB, Lee LP. Lab Chip. 2008; 8:2015–2031. [PubMed: 19023464]
19. Weigl B, Domingo G, LaBarre P, Gerlach J. Lab Chip. 2008; 8:1999–2014. [PubMed: 19023463]
20. Chin CD, Linder V, Sia SK. Lab Chip. 2007; 7:41–57. [PubMed: 17180204]
21. Soper S, Brown K, Ellington A, Frazier B, Garcia-Manero G, Gau V, Gutman S, Hayes DF, Korte B, Landers JL, Larson D, Ligler F, Majumdar A, Mascini M, Nolte D, Rosenzweig A, Wang J, Wilson D. Biosens Bioelectron. 2006; 21:1932–1942. [PubMed: 16473506]
22. Gervais L, Delamarche E. Lab Chip. 2009; 9:3330–3337. [PubMed: 19904397]
23. Ellerbee A, Philips S, Siegel AC, Mirica KA, Martinez AW, Striehl P, Jain N, Prentiss M, Whitesides GM. Anal Chem. 2009; 81:8447–8452. [PubMed: 19722495]
24. Jokerst JV, McDevitt JT. Nanomedicine. 2010; 5:143–155. [PubMed: 20025471]
25. Sun S, Yang M, Kostov Y, Rasooly A. Lab Chip. 2010; 10:2093–2100. [PubMed: 20544092]

26. Chin CD, Laksanasopin T, Cheung YK, Steinmiller D, Linder V, Parsa H, Wang J, Moore H, Rouse R, Umviligihozo G, Karita E, Mwambarangwe L, Braunstein SL, van de Wijgert J, Sahabo R, Justman J, El-Sadr W, Sia SK. Nat Med. 2011; 17:1015–1019. [PubMed: 21804541]
27. Herr AE, Hatch AV, Throckmorton DJ, Tran HM, Brennan JS, Giannobile WV, Singh AK. Proc Natl Acad Sci U S A. 2007; 104:5268–5273. [PubMed: 17374724]
28. Sia SK, Whitesides GM. Electrophoresis. 2003; 24:3563–3576. [PubMed: 14613181]
29. Chin CD, Linder V, Sia SK. Lab Chip. 2012; 12:2118–2134. [PubMed: 22344520]
30. Martinez WW, Phillips ST, Whitesides GM. Proc Natl Acad Sci USA. 2008; 19:606–611.
31. Cheng X, Irimia D, Dixon M, Sekine K, Demirci U, Zamir L, Tompkins RG, Rodriguez W, Toner M. Lab Chip. 2007; 7:170–178. [PubMed: 17268618]
32. Mao X, Huang T. Lab Chip. 2012; 12:1412–1416. [PubMed: 22406768]
33. Yager P, Edwards T, Fu E, Helton K, Nelson K, Tam MR, Weigl BH. Nature. 2006; 442:412–418. [PubMed: 16871209]
34. Rohrman BA, Richards-Kortum RR. Lab Chip. 2012; 12:3082–3088. [PubMed: 22733333]
35. Sun S, Ossandon M, Kostov Y, Rasooly A. Lab Chip. 2009; 9:3275–3281. [PubMed: 19865736]
36. Balsam J, Ossandon M, Kostov Y, Bruck HA, Rasooly A. Lab Chip. 2011; 11:941–949. [PubMed: 21243150]
37. Pamplona V, Passos E, Zizka J, Oliveira M, Lawson E, Clua E, Raskar R. CATRA: Cataract Probe with a Lightfield Display and a Snap-on Eyepiece for Mobile Phones, SIGGRAPH. 2011
38. McCall B, Pierce M, Graviss EA, Richards-Kortum R, Tkaczyk T. Tuberculosis. 2011; 91:S54–S60. [PubMed: 22079590]
39. Goldberg BD, Nezam SMRM, Jillella P, Bouma BE, Tearney GJ. Opt Express. 2009; 17:3619–3629. [PubMed: 19259202]
40. Ra H, Piyawattanametha W, Mandella MJ, Hsiung PL, Hardy J, Wang TD, Contag CH, Kino GS, Solgaard O. Opt Express. 2008; 16:7224–7232. [PubMed: 18545427]
41. Paturzo M, Finizio A, Memmolo P, Puglisi R, Balduzzi D, Galli A, Ferraro P. Lab Chip. 2012; 12:3073–3076. [PubMed: 22740323]
42. Matrecano M, Paturzo M, Finizio A, Ferraro P. Opt Lett. 2013; 38:896–898. [PubMed: 23503252]
43. Kim SP, Bose NK, Valenzuela HM. IEEE Trans Acoust Speech Signal Process. 1990; 38:1013–1027.
44. Kim SP, Su WY. IEEE Trans Image Process. 1993; 2:534–539. [PubMed: 18296238]
45. Tekalp, AM.; Ozkan, MK.; Sezan, MI. 1992 IEEE International Conference on Acoustics, Speech, and Signal Processing, 1992 ICASSP-92; 1992; p. 169-172.
46. Bates RHT, Cady FM. Opt Commun. 1980; 32:365–369.
47. Kuwamura S, Tsumuraya F, Miura, Baba N. Publ Astron Soc Pac. 2008; 120:348–357.
48. Gingras DJ, Aruga T. Opt Lett. 1990; 15:1380–1382. [PubMed: 19771097]
49. Mavandadi S, Dimitrov S, Feng S, Yu F, Yu R, Sikora U, Ozcan A. Lab Chip. 2012; 12(20):4102–4106. [PubMed: 22918378]
50. Mavandadi S, et al. PloS ONE. 2012; 7(5):e37245. [PubMed: 22606353]
51. Mavandadi S, Feng S, Yu F, Dimitrov S, Nielsen-Saines K, Prescott WR, Ozcan A. PloS ONE. 2012; 7(10):e46192. [PubMed: 23071544]
52. Goodman, JW. Introduction to Fourier Optics. Roberts & Company Publishers; Greenwood Village, CO, USA: 2005.
53. Brady, DJ. Optical Imaging and Spectroscopy. John Wiley & Sons; Hoboken, NJ, USA: 2009.

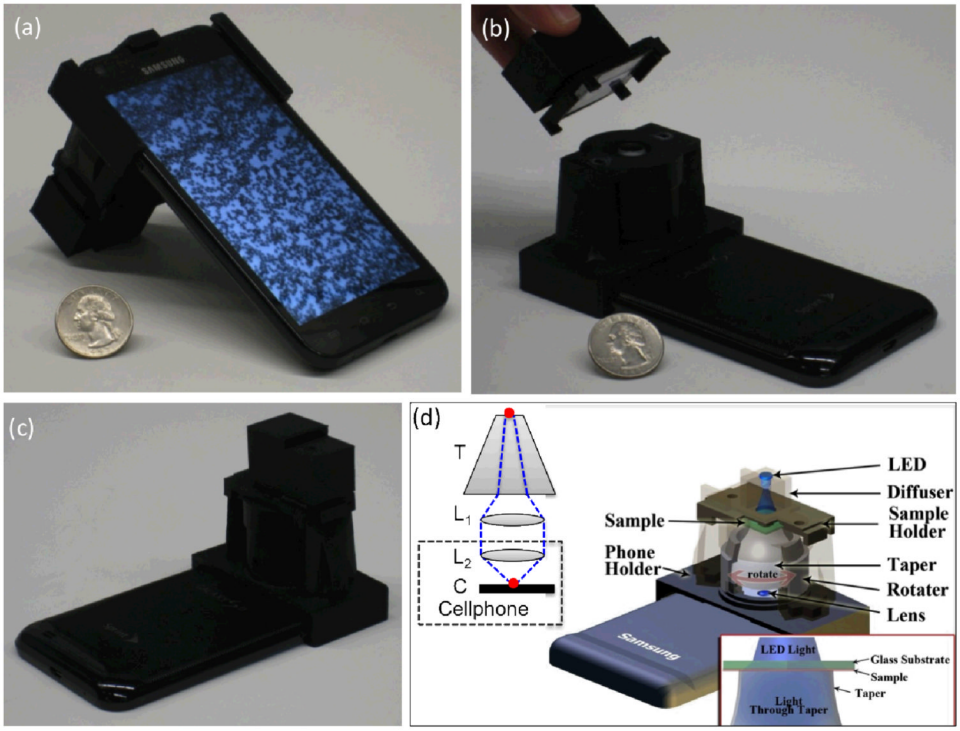

Fig. 1.

(a-c) Photographs of the *Contact Scope* installed on an Android cellphone from different views are shown. (d) Schematic diagram of the cellphone attachment of the *Contact Scope* is demonstrated, where the planar samples of interest are positioned in contact with the top facet of a tapered fiber-optic array (i.e., denoted as taper) and are illuminated by an incoherent light source (e.g., a simple LED). The transmission patterns of the micro-objects are magnified by the taper (T) and then imaged onto the cellphone CMOS chip (C) through an additional lens (L_1) and the built-in cellphone lens (L_2). Keeping the sample at a fixed position, the taper is rotated with discrete angular increments of e.g., 1-2 degrees, creating a sequence of raw contact images (e.g., ~10-40 frames) of the same sample. These raw images are then combined to create higher resolution final contact image, visualized through the smartphone screen.

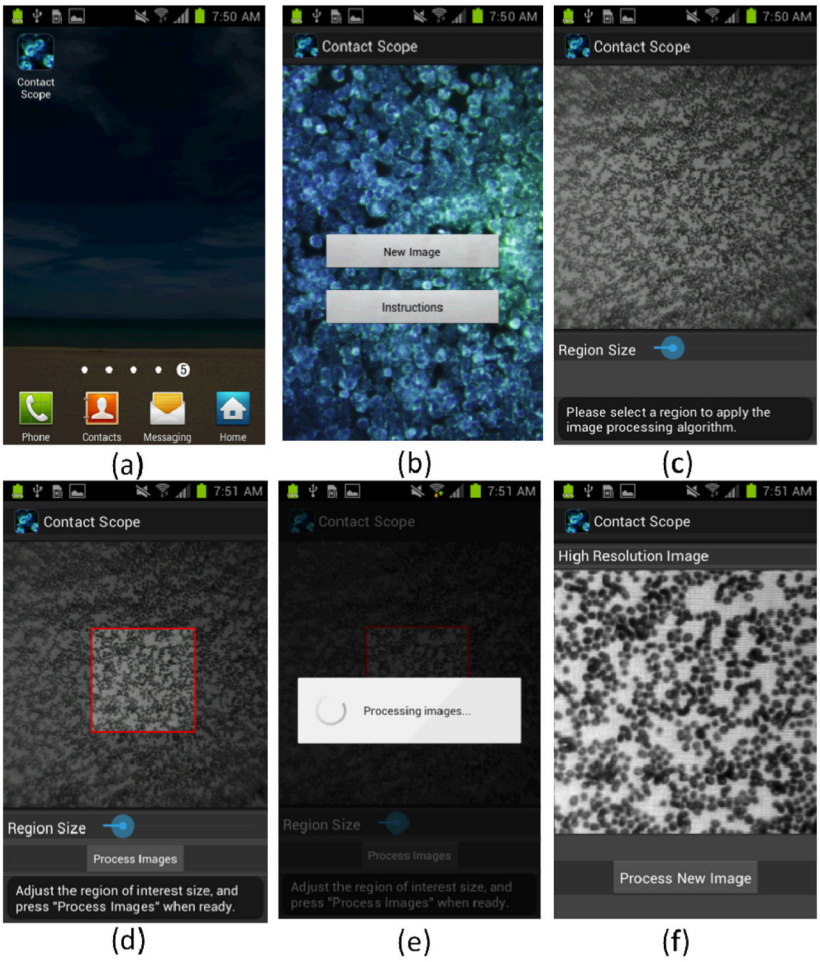

Fig. 2.

Screenshots of the *Contact Scope* application running on an Android phone is illustrated. (a) Once the user starts the application from the main menu, either *New Image* or *Instructions* can be selected. (b) Once *Instructions* tab is selected, the standard procedures for contact microscopy are displayed. Otherwise, if *New Image* is selected, the user is asked to rotate the fiber-optic taper with discrete angular increments of e.g., 1-2 degrees. The cellphone camera then captures a contact transmission image of the sample for each angular position of the fiber-optic taper and saves it on the memory of the phone, creating a series of contact images. (c) One of these raw contact images is displayed on the screen for the user to select a ROI. (d) The user can then adjust the size and the position of the selected ROI through finger movements performed on the cellphone screen. Once a ROI is defined, the user can click on the *Process images* tab to proceed with the digital processing of the raw transmission images. (e) While performing the shift-and-add algorithm through the cellphone, a small window pops up displaying '*Processing images*'. (f) The final contact image corresponding to the selected ROI is then displayed on the screen of the phone. If needed, the user can select the *Process New Images* tab to select another ROI of the same specimen.

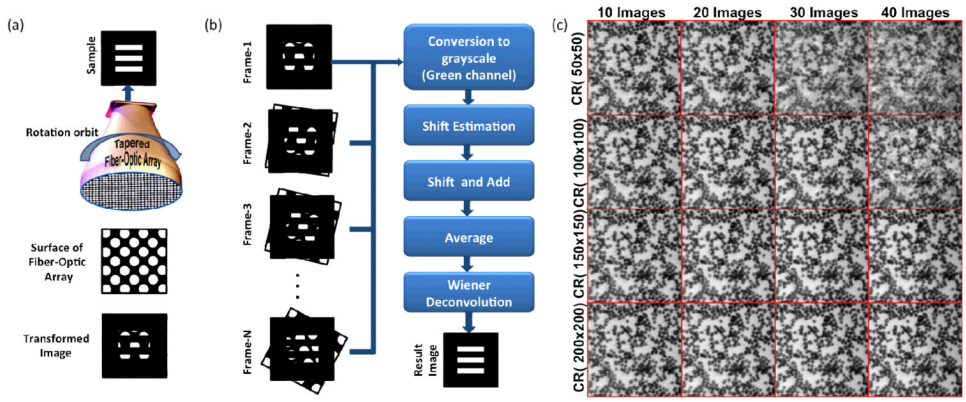

Fig. 3.

(a-b) Working principles of the *Contact Scope* are demonstrated, where a sample of interest is positioned on the top facet of a tapered fiber-optic array and is illuminated by an incoherent light source. The transmission pattern of the object is directly sampled by the top surface of the fiber-optic taper with an irregular pitch size of approximately ~ 2.5 μm, and is relayed toward the bottom facet of the fiber-optic array with an overall magnification factor of e.g., M~ 3. This magnified transmission pattern of the object is then imaged onto the cellphone CMOS chip through the use of an external lens. While keeping the sample and the cellphone camera at a fixed position, the tapered fiber-optic array component is manually rotated with discrete angular steps of e.g., 1-2 degrees. For each angular position of the fiber-optic array, a contact image is captured using the cellphone, creating a sequence of images for the same sample. To create a higher resolution image, these raw transmission images are then digitally merged based on an algorithm (b) as detailed in the Methods Section. (c) For a ROI of 300×300 pixels, containing red blood cells, the processed contact images are demonstrated as a function of (1) the correlation window (CR) size(ranging from 50×50 to 200×200 pixels), and (2) the number of raw frames(ranging from 10 to 40).

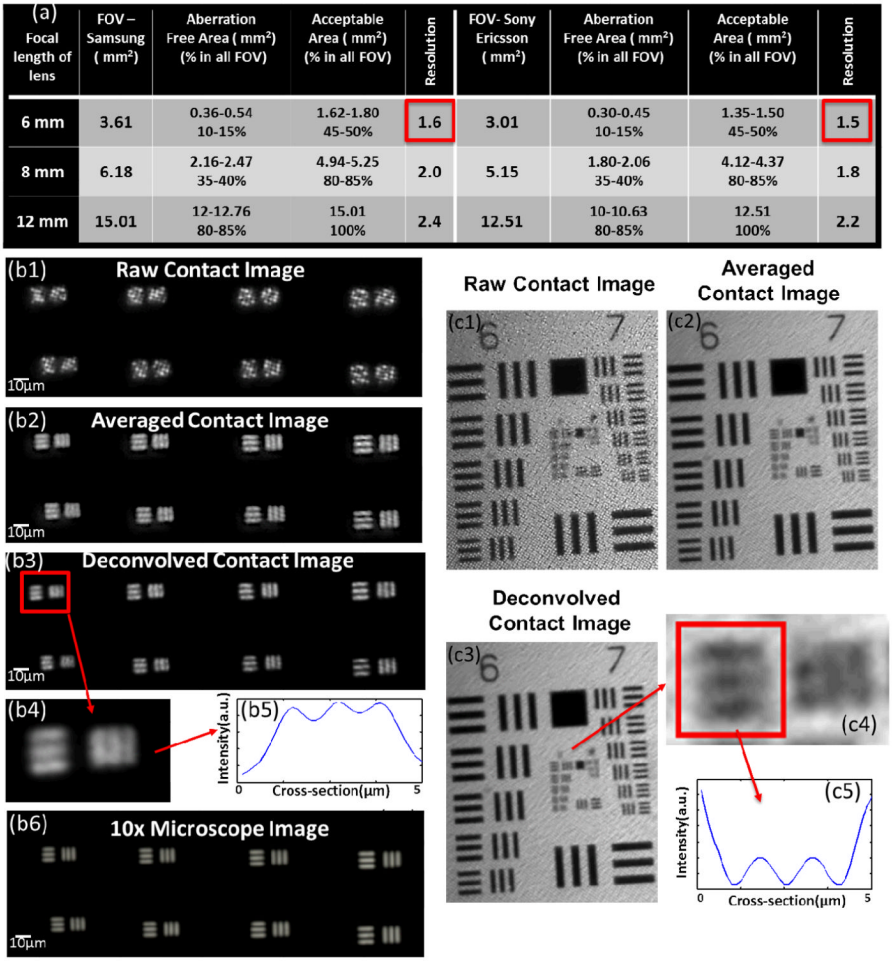

(a) Focal length of lens	FOV – Samsung (mm²)	Aberration Free Area (mm²) (% in all FOV)	Acceptable Area (mm²) (% in all FOV)	Resolution	FOV- Sony Ericsson (mm²)	Aberration Free Area (mm²) (% in all FOV)	Acceptable Area (mm²) (% in all FOV)	Resolution
6 mm	3.61	0.36-0.54 10-15%	1.62-1.80 45-50%	1.6	3.01	0.30-0.45 10-15%	1.35-1.50 45-50%	1.5
8 mm	6.18	2.16-2.47 35-40%	4.94-5.25 80-85%	2.0	5.15	1.80-2.06 35-40%	4.12-4.37 80-85%	1.8
12 mm	15.01	12-12.76 80-85%	15.01 100%	2.4	12.51	10-10.63 80-85%	12.51 100%	2.2

Fig. 4.

(a) Resolution and FOV comparison for two different cellphones (i.e., Samsung Galaxy and Sony-Ericsson) is provided as a function of the focal length of the external lens. (b1-6). A negative resolution target (i.e., a custom fabricated grating that has 1.6 μm to 2 μm line pairs from left to right) is imaged and processed through *Contact Scope*. (c1-3). A positive resolution target is also imaged and analyzed using the same contact microscopy platform, where the group 8 element 2 is resolved after the reconstruction as indicated by the cross section in the image (c4-5). Note that a CR of 150×150 pixels and 40 frames are used for the results presented in (a-c).

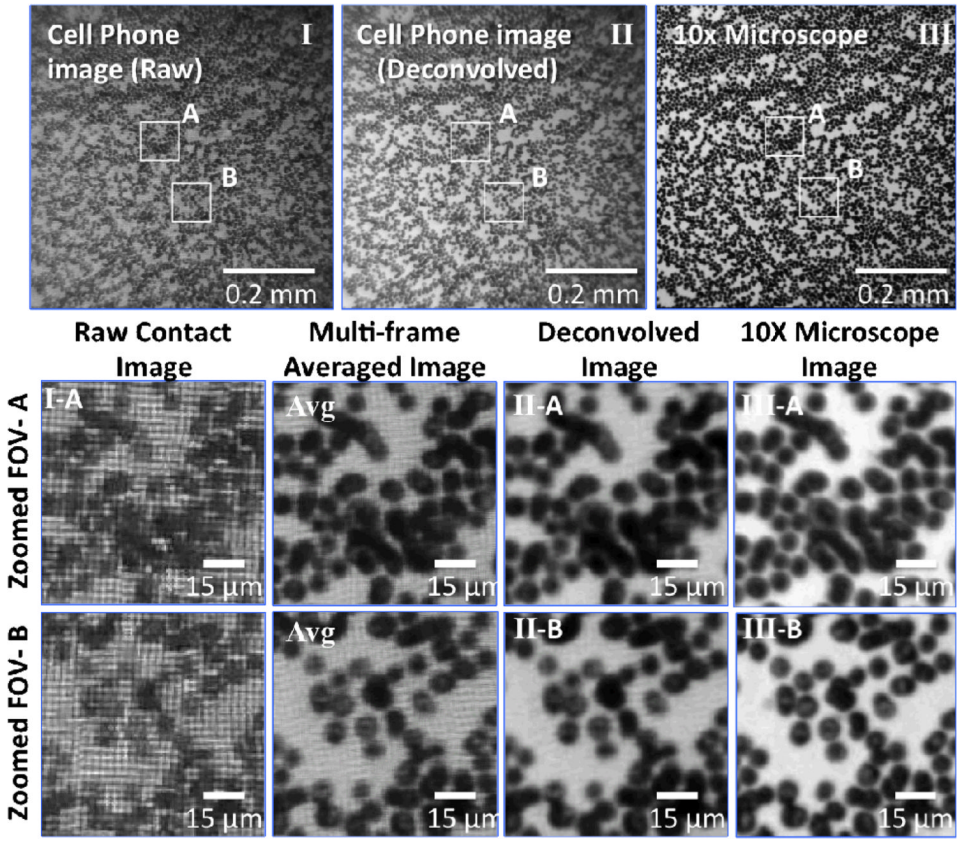

Fig. 5.

Wide-field images of a blood smear sample acquired using the *Contact Scope* (with the configuration employing a Samsung Android phone and a 6 mm add-on lens) is illustrated in (I), where the corresponding final high resolution contact image and a 10× microscope objective (NA = 0.25) comparison of the same FOV are also provided in (II) and (III), respectively. Two different FOVs (A-B) zoomed from (I-III) are also demonstrated, where raw contact images, multi-frame averaged images (using a CR of 150×150 pixels and 40 frames) and the final reconstructed images are compared against a 10× objective lens image. The raw contact images exhibit spatial artefacts that arise due to non-uniform sampling of the transmission intensity at the fiber optic array surface. These artefacts are digitally cleaned in the final processed image.

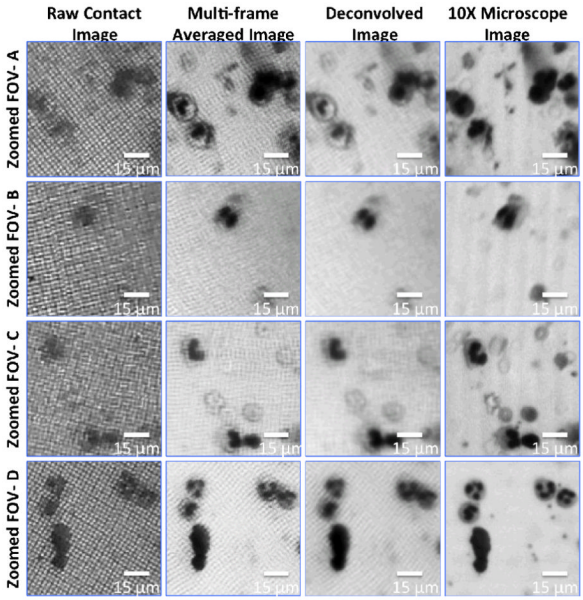

Fig. 6.
Same as in Figure 5, except for imaging of white blood cells.